Soft Matter

PAPER

View Article Online
View Journal | View Issue

Cite this: *Soft Matter*, 2024, **20**, 7715

Hydrodynamic thinning of a coating film induced by a small solid defect: evidence of a time–minimum thickness

Alice Etienne-Simonetti, [a] Frédéric Restagno, [a] Isabelle Cantat [b] and Emmanuelle Rio [a]

During coating processes, dust deposition can lead to an uneven thickness in the resulting film, posing significant problems in industrial processes. Our study explores the effects of solid defects using a vertical cylindrical fiber deposited on a silicone oil film coating a horizontal solid substrate. We use a hyperspectral camera to measure the film thickness by interferometry in the vicinity of the defect. As predicted and observed in many studies on various geometries, a circular groove appears around the fiber because of the capillary suction induced by the meniscus that grows at the bottom of the fiber. We measure the evolution of the thickness of the film at the groove over time. The thickness decreases and then increases again leading to the healing of the perturbation over time. We propose that healing is due to the arrest of the suction when the meniscus reaches its equilibrium shape. By combining geometric analysis with the thin film equation, we have developed scaling laws that predict both the minimum thickness of the groove, that we call the time–minimum thickness, and the time required to reach this minimum. If the time–minimum thickness reaches the thickness at which intermolecular forces begin to play a role prior to healing, the thickness of the groove will stop decreasing and saturate due to the competition between drainage and repulsive intermolecular forces. Based on the previous scaling law, we developed a scaling law accounting for the critical initial thickness of the film below which the intermolecular repulsion will start to have an effect, which is in good agreement with our experiments. These results thus offer valuable insights into predicting and preventing defects in coating processes, thereby improving the quality and reliability of coated products in various industries.

Received 7th March 2024,
Accepted 4th September 2024

DOI: 10.1039/d4sm00292j

rsc.li/soft-matter-journal

1 Introduction

Surface coating refers to the process of applying a layer or layers of a substance onto a surface to protect, improve, or decorate it. This process is used to enhance properties like the appearance of the surface, its corrosion, wear or scratch resistance, and its chemical stability. Among different possible coating techniques, such as chemical vapor deposition (CVD), physical vapor deposition (PVD), and electroplating, the use of a liquid is a cheap and common technique.[1] In this technique, surface coating typically involves spreading a liquid film, followed by a drying process.[2,3] Most applications, designed to confer chemical, optical, as well as mechanical properties to the surface, necessitate a film that is homogeneous in thickness at an optical scale. Nevertheless, spontaneous instabilities, such as the ribbing instability, can alter the film homogeneity by creating ribs while roll-coating[1,4] and various mechanisms can induce thickness heterogeneities through drying such as evaporation-induced instabilities,[5,6] evaporation inhomogeneities[7] or the coffee ring effect[8–10] in which particles set on the edges of the drop.

The presence of a defect at the liquid/air interface can increase these heterogeneities.[11–13] When a wetting sub-millimetric defect, such as a dust particle, is deposited on a film of micrometric thickness h_0, the meniscus rises around the dust particle. This phenomenon can be reproduced using a fiber of small radius r_f deposited vertically in contact with a liquid film coating a horizontal solid substrate. The equilibrium profile, which corresponds to the long-time situation, is a flat film connecting a meniscus. When the fiber radius is small compared to the capillary length, the equilibrium meniscus height scales as the fiber radius[14,15] and the thickness profile decreases continuously from this maximum to the flat film thickness h_0.

Upon contact between the fiber and the substrate, a small volume of liquid is displaced and forms an initial meniscus of strong negative curvature. Because of its low capillary pressure,

[a] *Solid-State Physics Laboratory, Orsay, France.*
E-mail: emmanuelle.rio@universite-paris-saclay.fr
[b] *Institute of Physics of Rennes, Rennes, France*

it then sucks the liquid from the film, rises on the fiber, and grows.[16–18] This suction creates a groove corresponding to the appearance of a minimum in the thickness profile $h(r,t)$, which is characterized by its thickness $h_g(t)$. Such a groove has been observed in many different situations and geometries as soon as a flat film is in contact with a meniscus: in soap films and soap bubbles, where the groove is also referred to as a dimple,[19–23] in coalescence problems,[24] as well as in inkjet printing[12] or in the case of solid objects on liquid deposited films.[13,16]

Aradian *et al.*[20] predicted the self-similar profiles achieved by the groove over time in a soap film or a wetting film, in the vicinity of a meniscus of constant radius. In the situation of a vertical fiber, the meniscus radius grows over time and its negative Laplace pressure decreases in the absolute value. Aradian's model therefore does not apply in this case, but the physical processes leading to a groove still hold. As the equilibrium profile achieved over time does not exhibit any minimum, the groove is only present in the transient regime. Consequently, $h_g(t)$ has a non-monotonic time dependency, reaching its minimum value $h_g^{\min}$ at $t_{\min}$. In this scenario, after $t_{\min}$, the film thinning stops, and the perturbation induced by the dust particles relaxes towards a meniscus of height comparable to the dust particle size. If $h_g^{\min}$ is smaller than h_{vdW} = 100 nm at which intermolecular forces start to play a role, the film dynamics may be affected by these forces before $t_{\min}$. The precise value of $h_g^{\min}$, and its comparison with h_{vdW}, thus determines the fate of the final coating.

In this work, we provide the first experimental evidence of the time–minimum groove thickness. We develop scaling laws for $h_g^{\min}$ and $t_{\min}$ in good agreement with our quantitative measurements. Additionally, we predict the critical film thickness below which the film will reach intermolecular repulsion forces.

2 Experimental setup and results

To observe the surface deformation in the vicinity of a cylindrical defect, we use a thin silicone oil film (HMS 301 Gelest) of viscosity η = 30 mPa s (at 25 °C), surface tension γ = 20 mN m^{-1} and density ρ = 980 kg m^{-3}. The capillary length is thus $l_c = \sqrt{\gamma/(\rho g)} = 1.4$ mm. A film of controlled thickness is deposited on a silicon wafer by spin-coating (Polos Spin 150i) at a rotation speed between 400 and 780 rpm during 30 seconds. We explore a range of initial thicknesses h_0 from 9 μm to 21 μm.

A vertical cylindrical glass fiber of radius r_f (Hilgenberg, radii from 100 μm to 500 μm) is fixed above the wafer, which is moved up with a lab jack. The wafer is covered by a Petri dish lid, in which a hole is drilled for the fiber to go through. The slow approach is stopped when the fiber begins to buckle, which makes sure that it is in contact with the wafer. As soon as this contact is made, the interference patterns provide a direct signature of the surface deformation (Fig. 1(b)). The circle of bright colors indicated by an arrow in Fig. 1(b) corresponds to the groove. This direct visualization shows that this groove remains axisymmetric, consistently with the good reproducibility of our groove measurements close to $t_{\min}$. Nevertheless, for the thicker

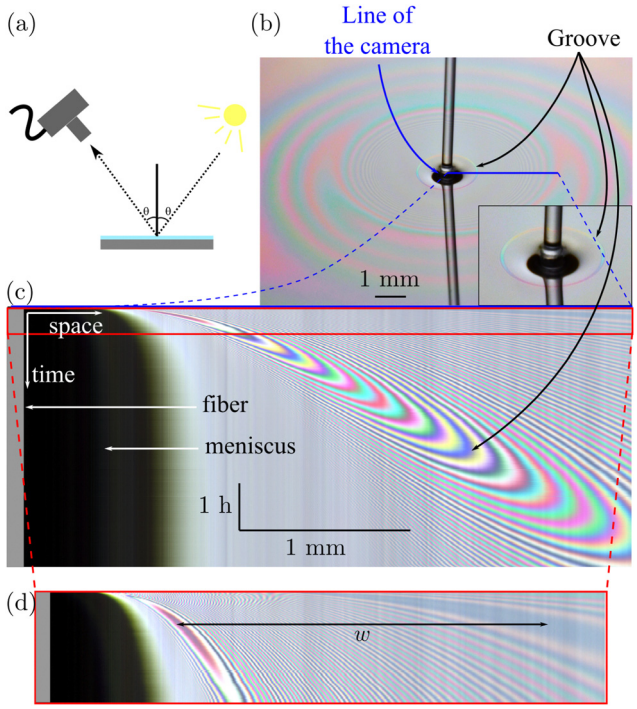

Fig. 1 (a) Experimental setup: a hyperspectral camera receives the reflection of a white LED light on a thin silicone oil film deposited on a wafer. (b) Photograph of the film after depositing the fiber on the wafer. The lower half of the fiber is a reflection on the wafer. One can see the surface deformation thanks to the thin film interferences and especially the colored circle that detaches from the rest, which corresponds to the groove. The observation line of the camera, materialized by a blue solid line, is set to be a radius of the system. (c) Space–time diagram of the colors of the film: the radius of the fiber is drawn in grey, the black region is the meniscus, next to it there is a grey region, where the thickness cannot be measured because the spectra are not resolved due to high thickness variation in space, then there is a thin colored region which is the groove, and then a series of fringes which correspond to the rest of the film. (d) Crop at early time of the space–time diagram above. The first colored region, the closest to the meniscus, where the colors do not vary much, is the groove. The pink region corresponds to the time minimum of the groove thickness, $h_g^{\min}$. The second flat colored region is the bump. The distance w between the bottom of the groove and the top of the bump is highlighted.

fibers, the buckling can result in a long-range asymmetric perturbation. Moreover, spin-coating results in a thicker film at the edge of the wafer, which will cause heterogeneities far from the fiber.

We measure quantitatively the film thickness along a line (blue solid line in Fig. 1(b)) thanks to a hyperspectral camera (Pika L-Resonon), receiving the reflection of a white LED fiber optic light (Dolan-Jenner Fiber-Lite Mi-LED) on the film (Fig. 1(a)). The camera is carefully oriented so that the line of measurement is along a radial direction. A hyperspectral camera is the equivalent of a line of spectrometers, which measures the spectrum of light for each point of the line the camera is aiming at. The camera software produces a space–time diagram of the colors of the film (Fig. 1(c)), with a light spectrum available at each pixel. We use the *oospectro* python library[25] to process the obtained spectra and compute the corresponding thicknesses with a precision of ±20 nm. The range of initial thicknesses that we can explore is limited. The camera spectral

resolution is too low to resolve the numerous oscillations of the spectra at higher thicknesses. The *oospectro* method prevents the measure of too small thicknesses, under 400 nm approximately. The possibility to measure the entire profile at all times determines our choice of the initial film thickness range: between h_0 = 8.4 μm and h_0 = 21 μm. We obtain the profile $h(r)$, with r the radial distance from the center of the fiber, determined as the middle of the black region at t = 0. r is known with a precision of 5 μm which is the resolution of the camera. In Fig. 1(c) the space–time diagram is cropped so that the first black pixel on the left corresponds to the edge of the fiber.

In Fig. 2(a), we plotted different thickness profiles for different times ranging from t = 0 h to t = 4.0 h. The origin of time is determined when the perturbation appears on the space–time diagram, the acquisition starting before making the contact. The precision of ±5 s is given by the frame rate of the camera. For all the times, we observed similar shapes for the profiles. At small r, *i.e.* close to the fiber (all the geometrical notations are defined in Fig. 4), and in the upper part of the meniscus, there are no points as the meniscus is too steep to measure the thickness. At the end of the meniscus, the thickness $h(r)$ decreases, goes through a minimum, and increases again. This space minimum corresponds to the bottom of the groove located at the position r_g and with a thickness $h_g(t)$. On the first recordable profile shown in Fig. 2(a), at t = 0 h, we can see that at r larger than r_g, the thickness increases and reaches a maximum (a bump) at r_b and then relaxes towards the flat part of the film. The positions $r_g(t)$ and $r_b(t)$ increase with time. Focusing on the groove at early times, in Fig. 2(b), we see that the groove first deepens until a thickness h_g^{min} and then fills back up. To quantify this space minimum, we extract the thickness at the bottom of the groove $h_g(t)$ from those thickness profiles and plot it against time as shown in Fig. 3(a). We see that the evolution of the groove thickness $h_g(t)$ is indeed non-monotonic and reaches its time minimum value h_g^{min} at the time t_{min}. This is the time–minimum thickness we mentioned in the introduction. In the discussion we will focus on this time–minimum thickness of the groove, h_g^{min}, and show that it is governed by the growth of the meniscus. In the following, all parameters X taken at this instance will be denoted X_{min} or X^{min}.

We can also extract the "width" of the groove w, defined as the distance between the bottom of the groove and the top of the bump, r_b–r_g. The measured value is extracted from the space–time diagrams as shown in Fig. 1(d). However, we can only measure w at early times (∼10 min) given that w grows over time (Fig. 3(b)) and the bump quickly goes out of the field of view of the camera.

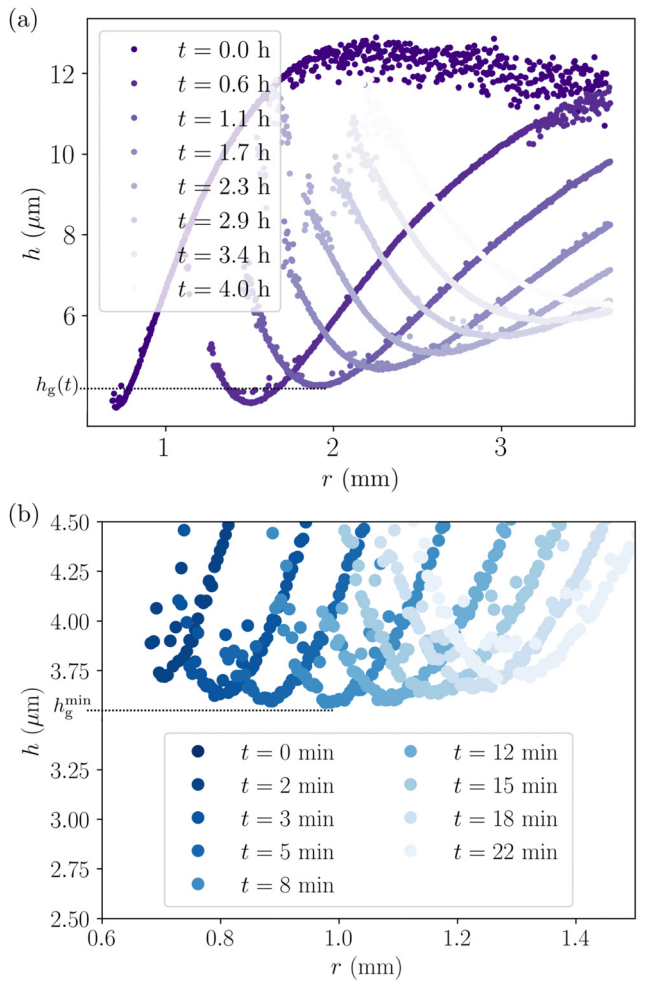

Fig. 2 (a) Typical thickness profiles: thickness of the film h as a function of the radial position r for different times (here for h_0 = 14.3 μm and r_f = 100 μm). t is known with an accuracy of 5 s, given the frame rate of the camera. Close to the fiber, the thickness decreases as we go down the meniscus. The film gets thinner till it reaches a minimum $h_g(t)$ at the bottom of the groove, and finally relaxes towards the flat part of the film of thickness h_0. The thickness is not measured at small r, which corresponds to the meniscus, because the profile is too steep. (b) Thickness profiles at early times zoomed in on the groove: the groove first deepens and then fills back up. h_g^{min} is the time–minimum thickness of the groove.

3 Discussion

Let us start with a description of the equilibrium shape of the meniscus. The height of the meniscus is fixed by the fiber radius r_f. Nevertheless, even for small fiber radii, the lateral extension far from the fiber is given by the capillary length l_c.[17,26] The semi-analytic expression of the entire profile in the limit of fiber of radius much smaller than the capillary length is $h^J(r)$, given in Section 6 from ref. 26.

$$h^J(r) = r_f\left[\ln\left(\frac{2r}{r+\sqrt{r^2-r_f^2}}\right) + K_0\left(\frac{r}{l_c}\right)\right], \qquad (1)$$

where K_0 is the modified Bessel function of the second kind of order 0. This profile is plotted in the inset of Fig. 4 for the three fiber radii we use. Its asymptotic behavior at a distance $r \gg r_f$ is $h^J \sim r_f K_0(r/l_c)$. We checked (not shown) that the equilibrium meniscus volume is dominated by this long-range behavior and, using $\int_0^\infty xK_0(x)\mathrm{d}x = 1$, we get

$$\Omega_m^{eq} \sim r_f l_c^2. \qquad (2)$$

The scaling of the radius of curvature of the static meniscus $r_{rz,eq}$ in the (r,z) plane will also be needed in the following.

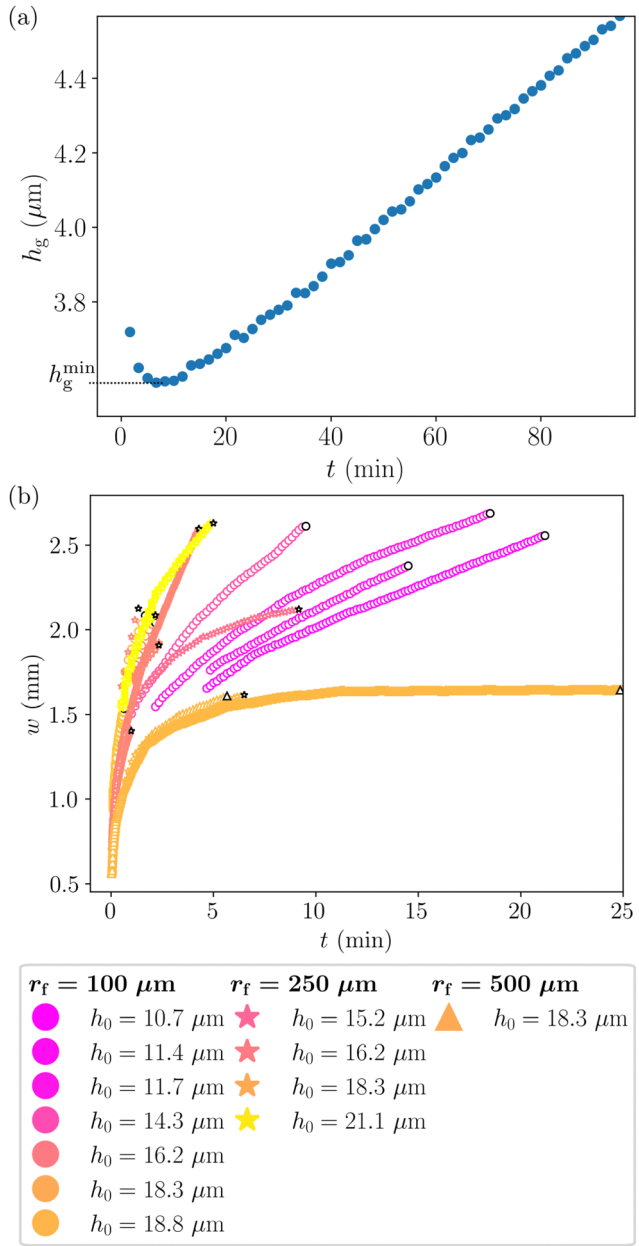

Fig. 3 (a) Typical time evolution of the thickness of the groove h_g (here for h_0 = 14.3 μm and r_f = 100 μm). First, the groove deepens, then it reaches a minimum, and finally, it fills back up again. (b) Width of the groove w over time for different initial thicknesses h_0 and fiber radii r_f: the groove gets wider with time and with thicker films. The black symbols are used to better distinguish the shapes of the symbols.

Close to the groove minimum, it is dominated by the last term of eqn (1) and scales as:

$$\frac{1}{r_{rz,eq}} \sim \frac{r_f}{l_c^2}. \quad (3)$$

Before reaching its equilibrium shape, the thin film is governed by the lubrication equation

$$\frac{\partial h}{\partial t} = \frac{\gamma}{3\eta}\nabla \cdot \left(h^3 \nabla \nabla^2 h\right). \quad (4)$$

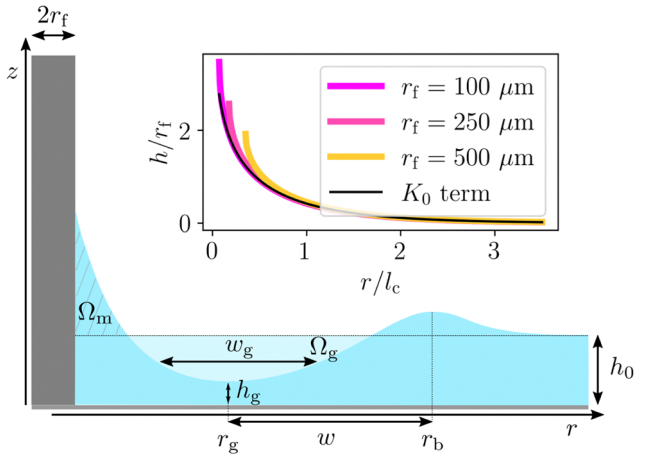

Fig. 4 Notations used in the models: r_f is the fiber radius, h_0 is the initial thickness of the film, w is the width of the groove, r_g is the position of the groove, r_b is the position of the bump, Ω_m is the volume of the meniscus, and Ω_g is the volume of the groove. (inset) Profile of the static meniscus computed with the equation of the interface from James[26] (Section 6). The black line is the asymptotic profile for $r \gg r_f$.

With a vertical characteristic length scale h_0, this equation directly imposes a scaling for the in-plane length scale, which has been proven to be valid in many different systems.[12,13,27,28] This scaling

$$w \sim \left(\frac{\gamma}{\eta} h_0^3 t\right)^{1/4}, \quad (5)$$

is also observed to rescale our data (Fig. 5). The different curves roughly collapse on a single master curve of slope 2.2 ± 0.45. For the fiber of radius 250 μm, the data are more dispersed than for the fiber of radius 100 μm. This is due to the fact that for several experiments for r_f = 250 μm, the perturbation is not perfectly axisymmetric around the fiber as previously discussed. Moreover, the edge effects discussed previously are probably the cause of some curves deviating from the straight line at later times.

However, in our specific situation, the film is in contact with a meniscus, whose radius of curvature r_{rz} introduces another length scale. The above scaling (eqn (5)) is therefore not the only possible one for in-plane lengths, and a more detailed study is required. The long-time behavior of an initially flat film in contact with a meniscus has been solved by Aradian *et al.*[20] In their case, the meniscus is invariant by translation in one direction and of constant radius of curvature. The scalings of our data will be obtained by adapting their results to our specific geometry.

In the geometry of Aradian *et al.*, the groove can be described through three characteristic length scales (denoted respectively l, h and w in ref. 20 and adapted to our notations in the following, with a superscript 'a'): the lateral extension of the perturbation w^a, the thickness at the minimum of the groove h_g^a and the in-plane characteristic length near the bottom of groove w_g^a (typically the groove width at $h = 2h_g^a$). The scaling obtained for w^a does not depend on the presence of

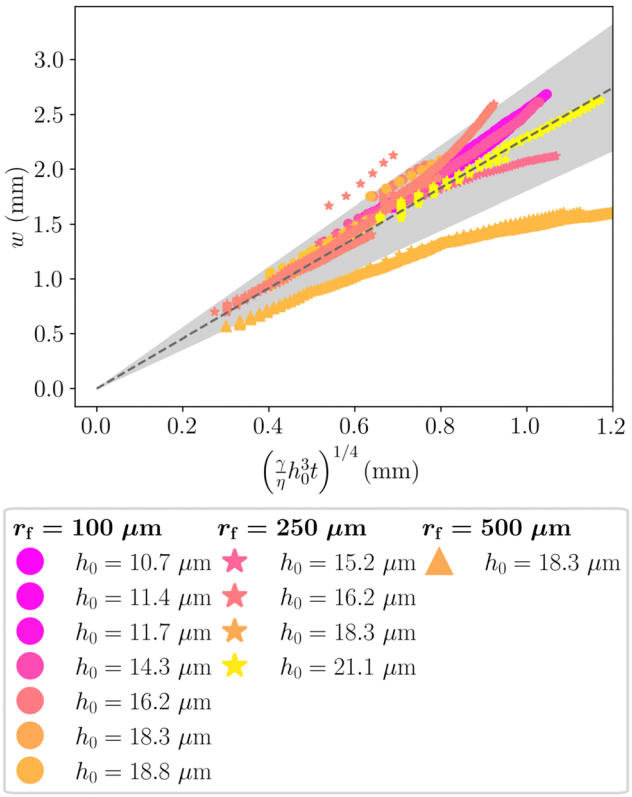

Fig. 5 Width of the groove w as a function of the scaling of w for different fiber radii r_f and initial thicknesses h_0: the data collapse on a master curve with slight scattering due to experimental conditions. The dashed line is the mean of the slopes resulting from the fits of each experiment; the coefficient of this slope is 2.2. The upper and lower slopes of the grey zone correspond to the slope of the dashed line plus or minus the standard deviation of all the slopes of the fits of each experiment, this standard deviation being 0.45.

the meniscus and the scaling of eqn (5) is recovered, consistently with our experimental observations. However, w_g^a scales differently and is obtained by (i) matching the film curvature on the left side of the groove with the meniscus curvature and (ii) matching the slopes on the right side of the groove. As the meniscus size depends on the time in our situation, the time scalings for w_g^a and h_g^a cannot be directly used. In particular, with a steady meniscus, the groove thickness h_g^a decreases as a function of time whereas in our situation $h_g(t)$ is non-monotonic. However, the matching conditions (i) and (ii) are true at each time and should remain valid in our case, leading to, respectively,

$$\frac{h_g}{{w_g}^2} \sim \frac{1}{r_{rz}}, \tag{6}$$

and

$$\frac{h_g}{w_g} \sim \frac{h_0}{w}. \tag{7}$$

These scalings impose that, at each time, the minimal thickness in the groove scales as

$$h_g \sim r_{rz}\left(\frac{h_0}{w}\right)^2 \tag{8}$$

4 Scaling laws for h_g^{min} and t_{min}

We propose to associate the conditions of eqn (8) with a volume conservation law to predict h_g^{min}. At time t_{min}, the capillary suction of the meniscus is overcome by the leveling process of the film, and we assume that the meniscus shape already scales as the equilibrium shape, so, using eqn (2), $\Omega_m^{min} \sim r_f {l_c}^2$. Indeed, in Fig. 1(c), one can see that at t_{min} the black zone, which is the meniscus width, has already reached 75% of its equilibrium value. On the other hand, the volume extracted from the groove at this time can be estimated as

$$\Omega_g^{min} \sim \pi((r_b^{min})^2 - (r_g^{min})^2)(h_0 - h_g^{min}), \tag{9}$$

with r_g^{min} and r_b^{min} respectively the positions of the groove and the bump at t_{min} (Fig. 4). We assume that the groove is very deep so $h_0 - h_g^{min} \sim h_0$ and that $w_{min} \sim r_b^{min}$, which leads to:

$$\Omega_g^{min} \sim h_0 {w_{min}}^2. \tag{10}$$

The volume conservation imposes that this volume extracted from the groove equals the sum of the meniscus and bump volumes. Assuming that the bump volume remains smaller than the meniscus volume (or at most of the same order), we find that Ω_m^{min} scales as Ω_g^{min}. The volume conservation can thus be expressed as $r_f {l_c}^2 \sim h_0 {w_{min}}^2$ which gives

$$w_{min} \sim l_c\left(\frac{r_f}{h_0}\right)^{1/2}. \tag{11}$$

This cannot be tested directly as the bump is outside the field of view of the camera at t_{min}, so we cannot measure w any longer.

We use eqn (8) at t_{min}, eqn (11), and the scaling of r_{rz} at equilibrium (eqn (3)) to build a scaling law for h_g^{min}:

$$h_g^{min} \sim \frac{{h_0}^2 {l_c}^2}{{w_{min}}^2 r_f} \sim \frac{{h_0}^3}{{r_f}^2}. \tag{12}$$

This scaling law describes well our data of the time–minimum thickness of the groove for different initial thicknesses and fiber radii (Fig. 6) as they collapse on a master curve. The dashed line is a fit of all the data and its slope is 14 which is of order-unity, and therefore the scaling law is validated.

Additionally, assuming that the scaling of w, given by eqn (5), still holds at t_{min}, and combining it with eqn (11), we get a scaling for t_{min}:

$$t_{min} \sim \frac{\eta}{\gamma}\frac{{r_f}^2 {l_c}^4}{{h_0}^5}. \tag{13}$$

This scaling is tested in Fig. 7. The data for different initial thicknesses h_0 and fiber radii r_f collapse on a master curve for the smallest fiber radii r_f = 100 μm and 250 μm. The dashed line is a straight line fit of these two data series. The surprisingly small slope of 1/162 could be attributed to the rough estimation of the volumes.

The data obtained with the fiber of radius r_f = 500 μm are significantly below the master curve. In this case, r_f gets close to

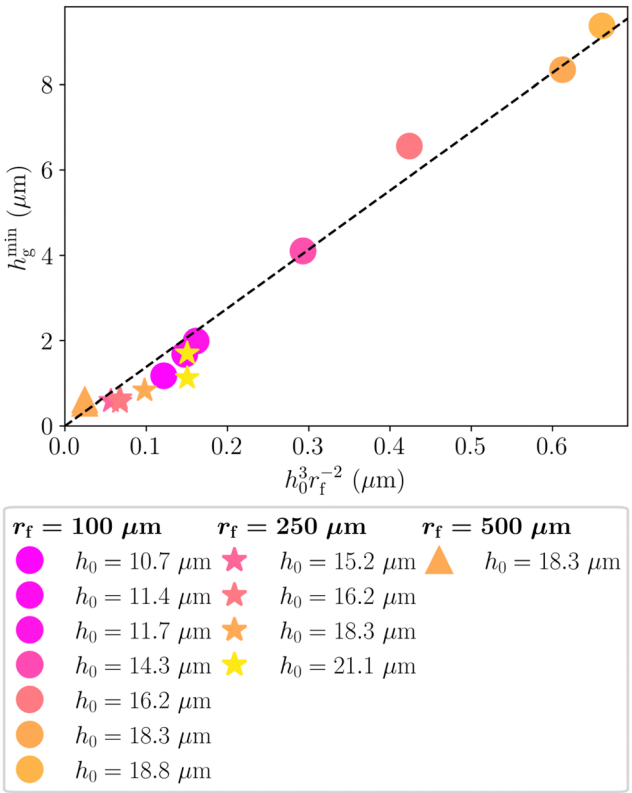

Fig. 6 Time minimum of the groove thickness h_g^{min} as a function of the theoretical value of h_g^{min} for different fiber radii r_f and initial thicknesses h_0. The dashed line is a fit of all the data, and the coefficient is 14.

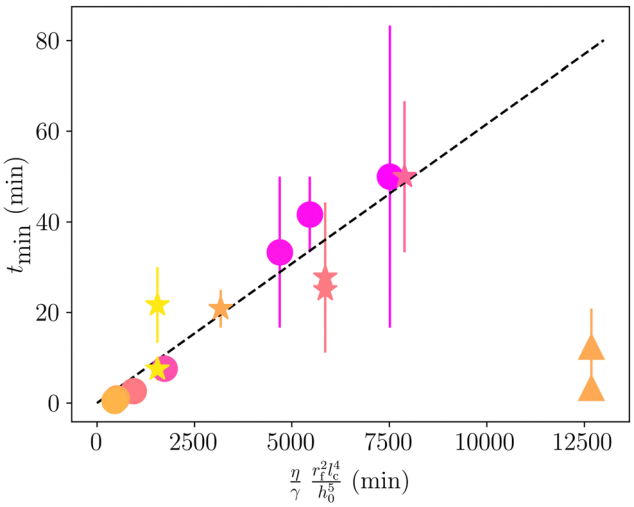

Fig. 7 Time t_{min} when the groove reaches its minimum thickness, as a function of the theoretical value of t_{min}, for different fiber radii r_f and initial thicknesses h_0. All data collapse on a master curve except the data for the largest fiber radius r_f = 500 μm as this radius gets close to the capillary length therefore the length scale separation begins to fail. The dashed line is a fit of all the data except r_f = 500 μm, the coefficient being 1/162. The error bars are estimated based on the width of the time interval at which we determine the time–minimum thickness. The legend is the same as in Fig. 6 on the left.

the capillary length (l_c = 1.4 mm), and the length scale separation begins to fail, which may explain this discrepancy.

5 Towards intermolecular repulsion

As h_g^{min} decreases with h_0, if we conduct experiments with even smaller initial thicknesses (smaller than 10 μm), we can expect h_g^{min} to reach a thickness at which the intermolecular forces start to play a role before or at t_{min}. To reach such small thicknesses, we have used a silicon oil with a smaller viscosity, η = 3 mPa s. Indeed, the process is so slow at small thicknesses with the viscous oil that the heterogeneities due to the spin-coating start to invade the film before t_{min}. For a less viscous oil, we sometimes obtain space–time diagrams that look like the one in Fig. 8. At early time, there is a groove very close to the meniscus; its colors are barely visible on the space–time diagram. At longer time, we see that a zone of almost uniform color (beige here) appears close to the meniscus which is the black area. It corresponds to a thin flat zone. To measure the thickness in this zone, we use the spectra measured using the hyperspectral camera. The thickness is too small to use the *oospectro* library to compute the thickness. Thus, we use the Sheludko renormalization.[29] It consists of inverting the function giving the intensity as a function of the thickness since it is bijective for small enough thicknesses. The measured thickness is of the order of 10 nm. We call this thin film a Newton film

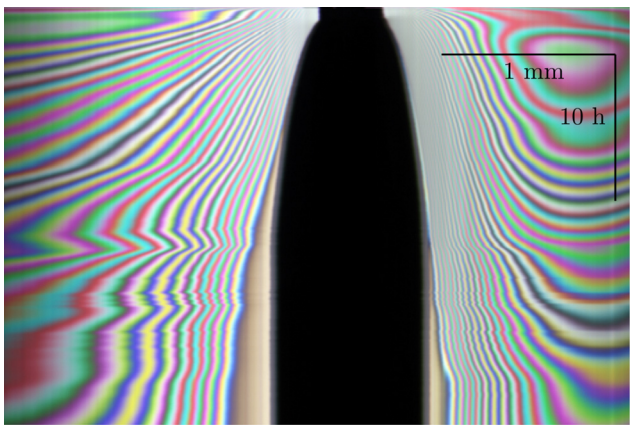

Fig. 8 Space–time diagram of a film which is a Newton film before t_{min}. The radius of the fiber is 250 μm and the initial thickness of the film is 5 μm. Close to the meniscus, we see a beige fringe that gets much larger than the other fringes. Before the beige fringe enlarges, there is a groove very close to the meniscus, which is difficult to see on the image.

with reference to the Newton black film in soap films, which necessitate repulsive forces to be stable.

We want to measure the critical initial thickness for which the groove will deepen enough (before t_{min}) to reach a thickness at which a Newton film appears. We built a phase diagram, plotted in Fig. 9, discriminating between experiments where a Newton film appears before t_{min} (in green) or does not appear before t_{min} (in red). t_{min} is determined *via* the scaling of eqn (13) and the coefficient from Fig. 7. Orange points are for experiments with r_f = 500 μm where t_{min} could not be

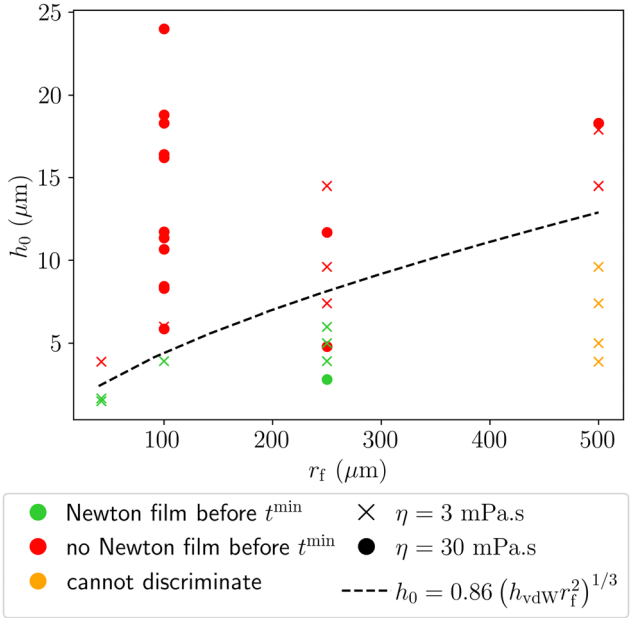

Fig. 9 Phase diagram of the film: the initial thicknesses h_0 are plotted against the fiber radii r_f. One point corresponds to one experiment. Crosses denote a viscosity η = 3 mPa s (PDMS) while full points stand for η = 30 mPa s (HMS 301 Gelest). The green points correspond to situations in which the Newton film appears before the groove reaches its minimum thickness (at t_{min}) and red points correspond to cases when there is no Newton film before t_{min}. t_{min} is determined *via* the scaling of eqn (13) and the coefficient from Fig. 7. Orange points are for experiments with r_f = 500 μm where t_{min} could not be determined theoretically as the scaling law was not validated for this fiber radius. The 42.5 μm radius fiber has been made by melting a 100 μm radius fiber from Hilgenberg. The dashed line is what we expect for the scaling of eqn (14). The coefficient comes from the fit of Fig. 10.

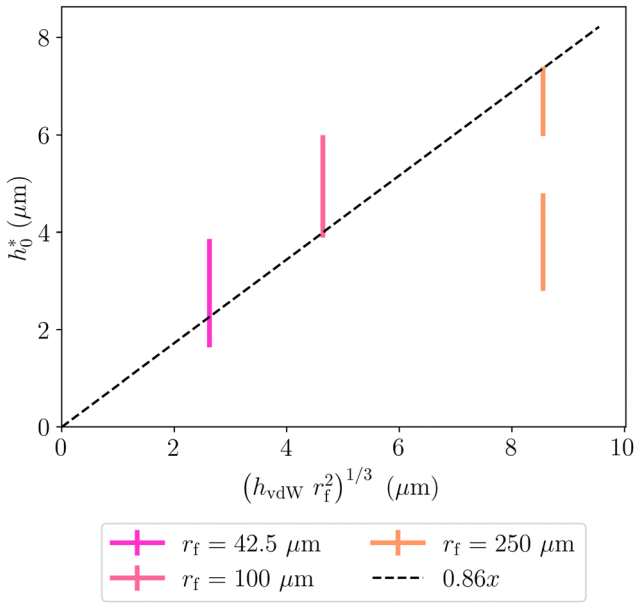

Fig. 10 Critical initial thickness h_0* for reaching the Newton film as a function of its scaling law, for different fiber radii r_f. The tops of the error bars are the minimum initial thicknesses h_0 for which the film exhibits a groove, and the bottoms of the error bars are the maximum initial thicknesses h_0 for which there is a Newton film. h_{vdW} is taken equal to 10 nm. The dashed line is a straight line fit of the middle of the error bars, the slope of which is 0.86. The two lines for r_f = 250 μm come from the two different viscosities used.

determined theoretically as the scaling law was not validated for this fiber radius. We call h_0* the thickness at which we observe a transition between the red and the green phase.

For silicone oil on a silicon wafer, the van der Waals forces between both interfaces are repulsive,[30,31] which may prevent the groove from thinning further. The thickness thus saturates to h_{vdW}, which explains the almost uniformly beige zone on the space–time diagram (Fig. 8). This situation is reached as soon as $h_g^{min} = h_{vdW}$. Using the scaling for h_g^{min} (eqn (12)) gives the critical initial thickness:

$$h_0^* \sim (h_{vdW} r_f^2)^{1/3}. \quad (14)$$

This scaling law is tested in Fig. 10. The data align on a straight line of slope 0.86 for h_{vdW} = 10 nm (measured previously), which confirms the scaling. This scaling law is also plotted in Fig. 9 as a dotted line and is in reasonable agreement with the experimental data.

6 Conclusions

To summarize, we have measured the evolution of the thickness of the groove, which appears around the meniscus created by a vertical cylindrical fiber on a thin silicone oil film. This groove propagates radially over time and its thickness exhibits a minimum in time. The width of this groove w is well described by a scaling law accounting for the flow which relaxes this perturbation using the thin film equation, as previously shown in various geometries. We build another scaling law for the time necessary to reach the time–minimum thickness of the groove assuming that the whole volume of the meniscus comes from the groove and that the time–minimum thickness of the groove is reached when the suction of the meniscus stops, that is to say at the equilibrium of the meniscus. This scaling law is in very good agreement with the measured values of t_{min}, except for the largest fiber because its radius gets comparable to the capillary length. Using geometric arguments on the shape of the groove, based on an asymptotic matching on each side of the groove, we obtain a scaling law for the time–minimum thickness of the groove h_g^{min}, which rescales our data.

For small initial thicknesses h_0, the groove reaches a thickness (~10 nm) at which intermolecular forces start to have an effect and the space–time diagrams exhibit a large zone where the thickness is uniform corresponding to a thin flat zone. Based on the scaling law for h_g^{min}, we deduce a scaling law for the critical initial thickness h_0* below which disjoining repulsion forces will play a role. Experimental data are well described by this prediction.

As for perspectives, the dynamics of the groove while going down and then up are still open questions, as well as the Newton film dynamics: enlargement velocity, influence of the

nature of the substrate *etc.* Moreover, drying could be added to the system to mimic the industrial coating problem.

Author contributions

I. C., A. E.-S., F. R. and E. R. designed the experimental study. A. E.-S. carried out the experiments. I. C., A. E.-S., F. R. and E. R. analyzed and interpreted the experimental results and wrote the manuscript.

Data availability

Data for this article are available at **https://doi.org/10.5281/zenodo.12801627**.

Conflicts of interest

There are no conflicts to declare.

Acknowledgements

This research was funded by the Agence Nationale de la Recherche (ANR), grant ANR-20-CE30-0019 (DRAINFILM). A CC BY license is applied to the AAM arising from this submission, in accordance with the grants open access conditions. We thank Arnaud Antkowiak and Théophile Gaichies for fruitful discussions.

Notes and references

1 K. J. Ruschak, *Annu. Rev. Fluid Mech.*, 1985, **17**, 65–89.
2 A. Oron, S. H. Davis and S. G. Bankoff, *Rev. Mod. Phys.*, 1997, **69**, 931.
3 P. M. Schweizer and S. Kistler, *Liquid Film Coating: Scientific principles and their technological implications*, Springer Science & Business Media, 2012.
4 F. V. Lopez, L. Pauchard, M. Rosen and M. Rabaud, *J. Non-Newtonian Fluid Mech.*, 2002, **103**, 123–139.
5 Q. Magdelaine-Guillot de Suduiraut, PhD thesis, Sorbonne université, 2019.
6 C. Robert, PhD thesis, Sorbonne université, 2022.
7 A. Faidherbe, M. Wilmet, J. Teisseire, F. Lequeux and L. Talini, *Langmuir*, 2023, **39**, 3018–3028.
8 R. D. Deegan, O. Bakajin, T. F. Dupont, G. Huber, S. R. Nagel and T. A. Witten, *Nature*, 1997, **389**, 827–829.
9 H. Kim, F. Boulogne, E. Um, I. Jacobi, E. Button and H. A. Stone, *Phys. Rev. Lett.*, 2016, **116**, 124501.
10 M. Corpart, F. Restagno and F. Boulogne, *J. Fluid Mech.*, 2023, **957**, A24.
11 M. Jalaal, C. Seyfert and J. H. Snoeijer, *J. Fluid Mech.*, 2019, **880**, 430–440.
12 M. A. Hack, M. Costalonga, T. Segers, S. Karpitschka, H. Wijshoff and J. H. Snoeijer, *Appl. Phys. Lett.*, 2018, **113**, 183701.
13 D. Garcia-Gonzalez, M. A. Hack, M. Kappl, H.-J. Butt and J. H. Snoeijer, *Soft Matter*, 2023, **19**, 1241–1248.
14 D. Quéré and J.-M. Di Meglio, *Adv. Colloid Interface Sci.*, 1994, **48**, 141–150.
15 D. F. James, *J. Fluid Mech.*, 1974, **63**, 657–664.
16 M. l'Estimé, PhD thesis, Sorbonne université, 2021.
17 C. Clanet and D. Quéré, *J. Fluid Mech.*, 2002, **460**, 131–149.
18 S. Guo, X. Xu, T. Qian, Y. Di, M. Doi and P. Tong, *J. Fluid Mech.*, 2019, **865**, 650–680.
19 D. Platikanov, *J. Phys. Chem.*, 1964, **68**, 3619–3624.
20 A. Aradian, E. Raphael and P.-G. De Gennes, *EPL*, 2001, **55**, 834.
21 O. Atasi, D. Legendre, B. Haut, R. Zenit and B. Scheid, *Langmuir*, 2020, **36**, 7749–7764.
22 A. Gros, A. Bussonnière, S. Nath and I. Cantat, *Phys. Rev. Fluids*, 2021, **6**, 024004.
23 J. Miguet, M. Pasquet, F. Rouyer, Y. Fang and E. Rio, *Phys. Rev. Fluids*, 2021, **6**, L101601.
24 D. Y. C. Chan, E. Klaseboer and R. Manica, *Soft Matter*, 2011, **7**, 2235–2264.
25 F. Boulogne, *Oospectro*, **https://oospectro.readthedocs.io/en/latest/**.
26 D. F. James, *J. Fluid Mech.*, 1974, **63**, 657–664.
27 S. Lakshman, W. Tewes, K. Harth, J. H. Snoeijer and D. Lohse, *J. Fluid Mech.*, 2021, **920**, A3.
28 J. D. McGraw, T. Salez, O. Bäumchen, E. Raphaël and K. Dalnoki-Veress, *Phys. Rev. Lett.*, 2012, **109**, 128303.
29 A. Sheludko, *Adv. Colloid Interface Sci.*, 1967, **1**, 391–464.
30 L. Léger and J. F. Joanny, *Rep. Prog. Phys.*, 1992, **55**, 431–486.
31 A. Cazabat, S. Gerdes, M. Valignat and S. Villette, *Interface Sci.*, 1997, **5**, 129–139.

